Journal of Mathematical Sciences and Modelling, *7(2) (2024) 90-111*
Research Article

Journal of Mathematical Sciences and Modelling

Journal Homepage: www.dergipark.gov.tr/jmsm
ISSN: 2636-8692
DOI: https://doi.org/10.33187/jmsm.1505481

Modeling and Analysis of Kamikaze *UAV* Design with 3 Different Wing Configurations

Ahmed Receb Demirel[1], **Mustafa Murat Yavuz**[2] **and Nehir Tokgöz**[1*]

[1]*Faculty of Engineering, Sakarya University, Sakarya, Türkiye*
[2]*Faculty of Engineering, Izmir Democracy University, Izmir, Türkiye*
[*]*Corresponding author*

Article Info

Keywords: *Angle of Attack, Kamikaze, UAV, Pressure*
2010 AMS: *39A13, 39A28, 39A30, 92D30*
Received: *26 June 2024*
Accepted: *15 August 2024*
Available online: *28 August 2024*

Abstract

Appropriate design parameters need to be determined for unmanned aerial vehicles that can perform kamikaze missions. In this study, a *UAV* with 3 different wing configurations and a fuselage and tail wings were designed, and the flow around the wing was examined using computational fluid mechanics. Advanced modeling techniques were employed to simulate and analyze the aerodynamic behavior of these configurations. The effect of angle of attack (AoA), wing positioning on the fuselage, and wing configurations were investigated. Due to the effect of the wing sweep angle, high-pressure values in the arrow-angle wing were lower than in rectangular and trapezoidal wings. In a similar situation, the flow separation on the arrow-angle wing is less advanced towards the wing tip. When the wing type and connection location were examined, the highest C_l/C_d ratio was obtained in the trapezoidal model connected to the fuselage in the middle. The results of numerical wing models compared with the theoretical lift coefficient were consistent. Trapezoidal and rectangular wings had a high lift coefficient, but after 15° of AoA, the lift coefficient decreased. At angles of attack beyond 15°, the arrow-angle wing still has an increasing lift coefficient. As the angle of attack increased, the drag coefficient was also enhanced. The lowest drag coefficient occurred in the arrow-angle wing model. Up to $5^\circ$of AoA, all wing models raised the C_l/C_d ratio. The C_l/C_d ratio decreased at higher angles of attack. As a result of the examination, it would be more correct to choose trapezoidal and arrow-angle wings.

1. Introduction

Unmanned aerial vehicles (*UAVs*), often colloquially termed drones, represent a class of aircraft capable of autonomous flight without human intervention. The evolution of *UAVs* has been spurred by the progressive complexity and advancements within the domains of control systems, robotics, electronics, and artificial intelligence [1]. These technological strides have profoundly influenced the design, production, and versatility of drones, broadening their applications across numerous industries and sectors. *UAVs* are now extensively employed in logistics [2,3], agriculture (including crop protection) [4], construction site monitoring, cinematography [5,6], surveillance operations [7], smart city initiatives [8], disaster response efforts [9], healthcare logistics, online shopping transportation [10], remote sensing missions [11], and provision of wireless connectivity [12]. This multifaceted utility underscores the pivotal role that *UAVs* play in modern society, revolutionizing various fields through their unparalleled aerial capabilities. The versatile applications of drones, a technology drawing significant interest and continuously progressing, have emerged as unexpectedly powerful tools, even in the Ukrainian conflict [13]. Notably, *UAVs* are employed for tasks such as crowd monitoring, dissemination of public information, and sanitization efforts aimed at combating the COVID-19 pandemic [14]. Furthermore, efforts are underway to develop methods for utilizing authorized *UAVs* in tracking and surveilling potentially threatening unmanned aerial vehicles, demonstrating the ongoing innovation and adaptability within the realm of drone technology [15]. The adoption of drones has revolutionized the execution of monotonous, hazardous and labor-intensive tasks, offering enhanced efficiency and reduced expenses while mitigating risks to human safety [16]. By substituting traditional methods with drones, substantial cost savings can be achieved alongside widespread acceptance, while also augmenting the value of collected data [17].

Email addresses and ORCID numbers**: ahmedrecebd@gmail.com, 0009-0002-5120-3353 (A. R. Demirel), murat.yavuz@idu.edu.tr, 0000-0002-5892-0075 (M. M. Yavuz), nehirtokgoz@sakarya.edu.tr, 0000-0001-9264-9971 (N. Tokgöz)**

Cite as "A. R. Demirel, M. M. Yavuz, N. Tokgöz, *Modeling and analysis of Kamikaze UAV design with 3 different wing configurations*, J. Math. Sci. Model., 7(2) (2024), 90-111"

With their affordability and heightened maneuverability, adaptability, safety features, and customization options, drones have become indispensable tools [18, 19]. Recent studies indicate a remarkable growth trajectory in the global drone market, with projections soaring to \$19.85 billion USD by 2021, marking a compound annual growth rate of nearly 13% over the forecast period [20]. Nonetheless, it is essential to acknowledge the mounting concerns regarding cybersecurity associated with drone applications. A significant constraint for drones revolves around their range and autonomy, which are influenced by factors such as battery capacity and aerodynamic performance [20]. Over recent years, various approaches have been explored to enhance drone efficiency, with particular focus on methods like implementing winglets [21]. Prieto et al. [13] conducted an aerodynamic enhancement of a "Vertical Take Off and Landing" drone by integrating winglets and wingtips. They evaluated two approaches for this analysis: the Vortex Lattice Method and Computational Fluid Dynamics modeling. By comparing the results from OpenFOAM and XFLR5, it was observed that, XFLR5 tends to overestimate lift and viscous drag while underestimating induced and total drag. Quintana et. al [22], introduced and examined an optimized morphing unmanned aerial vehicle (UAV) designed to dynamically adjust, and extend its wings for enhanced aerodynamic and structural performance. Their study aimed to assess and enhance the *UAV's* efficiency, analyze flight transition dynamics, and ensure structural integrity. The modal analysis results indicated that, the wing's low natural frequency increases the likelihood of flutter and vibratory response induced by aerodynamic forces and disturbances. Voskuijl [23] conducted a study to offer an in-depth technical analysis of the current stray munitions, focusing on their design and the performance of the aircraft that deploy them. To achieve this goal, the scientist created a detailed database of stray munitions using information sourced from publicly available data. Six primary configurations were identified: (1) conventional, (2) delta wing, (3) tandem wing, (4) canard, (5) cruciform and (6) rotorcraft. According to the results, the cruciform configuration was beneficial for precise flight path control. The tandem wing configuration integrated the advantages of a canister launch with high aspect ratio wings, making it suitable for long-range flights, while the delta wing design provided a large internal volume and reaches high terminal attack airspeed. Zampronha et al. [24] examined the Iranian HESA Shahed 136 drone to explore recent advancements in low-cost, long-range precision weapons, with a focus on kamikaze drones and stray munitions. The HESA Shahed 136 has transformed the approach to precise long-range strikes a capability previously exclusive to costly and technologically sophisticated tactical missiles and aircraft. Now, this function can be performed with inexpensive drones, igniting arms race not only to develop the most advanced and precise weaponry, but also to create the most affordable solution. Experimental analysis was carried out by Saraçyakupoğlu et al. [25] within the framework of four different scenarios to calculate the *UAV* and determine the design criteria. The *UAV* under discussion was designed with extensive operational capability, particularly suited for defense and border security tasks. The research suggested that the *UAV's* mid-wing, double-tail design, along with its relatively light body, enhanced its three-axis stability, providing notable benefits, particularly concerning operational cost. In the study conducted by Sakarya et al. [26], the aim was to develop an unmanned helicopter project that could be used in the military field. The helicopter they developed, which can be controlled autonomously or by a pilot, was designed for areas, where soldier visibility or access is difficult and dangerous. It is a prototype product intended for aerial reconnaissance, surveillance, and, in certain situations, it can perform a suicide dive thanks to the explosive it carries.

The literature review clearly indicates a growing momentum in the research and development of drones and model airplane-sized unmanned aerial vehicles (*UAVs*). These studies have predominantly focused on advancing the design and functionality of *UAVs*, driven by the increasing demand for innovative applications across various industries. In this study, we have sought to contribute to this evolving field by developing a novel unmanned aerial vehicle with a distinctive usage area, employing advanced numerical methods. A comprehensive analysis was conducted to investigate the impact of the wing structure and the positioning of the wing/fuselage joint on the *UAV's* performance. This approach not only aims to enhance the aerodynamic efficiency of the *UAV* but also to explore new design possibilities that could expand its operational capabilities.

2. Material and Method

2.1. Design parameters and models

The design consists of the fuselage, fuselage wing, and tail wing. In general, a parametric formula regarding body length was used. In the parametric formula taken from the literature, homemade composites were chosen due to their lightness and ease of production, and alpha and C coefficients were used as 3.50 and 0.23 [27-28]. The maximum aircraft length value, generally 6 kg, is calculated in Eq. (2.1) and Eq. (2.2) below. According to the result obtained from Eq. (2.2), the body length should not exceed 1.932 $meters$. The hull length for the design was determined as 1.850 $meters$. The width of the body is 0.210 $meters$ and the height is 0.205 $meters$. The body design of the kamikaze *UAV* model is shown in Figure 2.1.

$$\begin{aligned} W_0 &= 6kg = 13.23Ib && (2.1)\\ length\,(feet) &= a \times W_0^c = 3.5 \times 13.23^{0,23} = 6.339feet = 1.932m && (2.2)\end{aligned}$$

According to the result obtained from Eq. (2.2), the body length should not exceed 1.932 $meters$. The hull length for the design was determined as 1.850 $meters$. The width of the body is 0.210 $meters$, and the height is 0.205 $meters$. The body design of the kamikaze *UAV* model is shown in Figure 2.1

After determining the fuselage dimensions, the wingspan ratio (AR) must first be determined for wingspan sizing. This ratio varies depending on the aircraft type. C_d is a dimensionless parameter used to measure the drag of a wing. The C_d coefficient is a function of the angle of attack (AoA). As the angle of attack increases, the C_d coefficient increases and therefore more thrust is required. Drag coefficient; C_d [2];

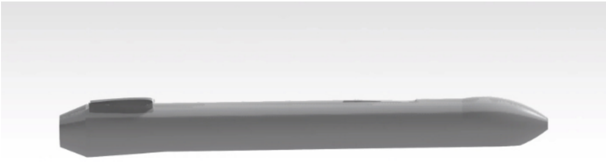

Figure 2.1: Kamikaze *UAV* body design

$$C_d = \frac{(2 \times D)}{(\rho \times V^2 \times S)} \tag{2.3}$$

In this equation, D: drag force (N), ρ: density of air $\left(1.225\, kg/m^3\right)$, V: speed (m/s), S: wing area m^2. Wing taper can change wing lift distribution. This is assumed to be an advantage of the taper, as it is a technical means to improve lift distribution. The aspect ratio of the wing was used as a span ratio of 7.27, within the range of 5-9 ratio used in general aviation structure. Technical drawings and basic dimensions for arrow-angle, trapezoidal and rectangular wings were shown in Figure 2.2. Basic geometrical properties of the wings were given in the Table 2.1.

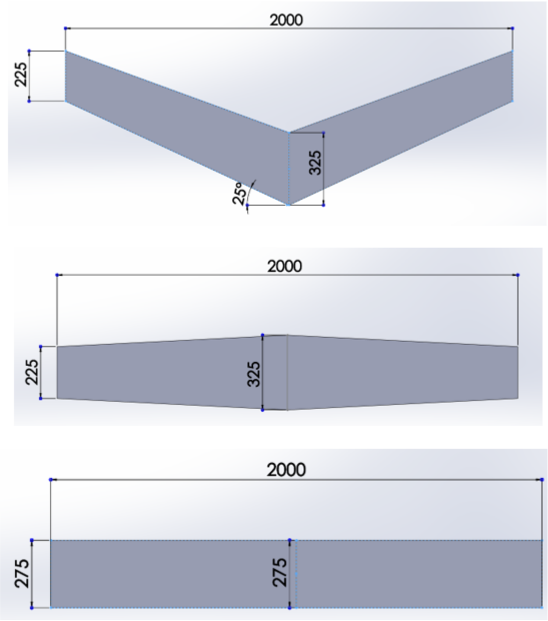

Figure 2.2: Arrow-angle, trapezoidal and rectangular Wings (all lengths (mm))

NACA 4412 profile was preferred on the wings due to its ability to provide high lift force at small angles of attack at relatively low Reynolds numbers, and NACA 0012 profile, which does not contain an asymmetrical situation due to stabilization control in the tail, was preferred. V-tail geometry was used in the tail and a rear-wheel drive propeller was preferred. Reynolds number is the ratio of inertial forces to viscosity forces of a fluid, and this value gives the relative importance of these two types of forces to each other under a certain flow condition.

Table 2.1: Wing geometry dimensions

Wing	Arrow-angle (mm)	Trapezoidal (mm)	Rectangular (mm)
$c_{root}\,(Root\ chord\ length)$	325	325	275
$c_{tip}\,(Tip\ chord\ length)$	225	225	275
$c_{ave}\,(Ave.chord\ length) = \frac{c_{root}+c_{tip}}{2}$	275	275	275
$b\ (Wing\,span)$	2000	2000	2000
$AR = b/c_{ort}$	7.27	7.27	7.27
$S\,(Wing\,area) = b \times c_{ort}$	0.55	0.55	0.55
$\lambda\ (Tapering\ rate) = c_{tip}/c_{root}$	0.6923	0.6923	1
λ	1	1	1
$c_{mgc}\,(Average\,aerodynamic\,chord\,length) = (2/3) \times c_{root} \times \left(1+\lambda+\lambda^2/(1+\lambda)\right)$	170.51	170.51	275

Therefore, the Reynolds number is frequently used to characterize different flow regimes, such as uniform flow and turbulent flow. The given formula (2.4) is used for calculation of Reynolds number;

$$Re = \frac{\rho \times V \times L}{\mu} = \frac{V \times L}{v} \tag{2.4}$$

$\rho =$ density $\left(kg/m^3\right)$
$V =$ flow velocity $\left(m/s^2\right)$
$L =$ the length of the pipe through which the fluid flows (m)
$\mu =$ dynamic viscosity of the fluid $(Pa.s)$
$v =$ kinematic viscosity of the fluid $\left(m^2/s\right)$

Based on the equation, it can be decided whether the flow is laminar or turbulent. Reynolds number value ranges for external flow (Eq. (2.5) and (2.6)) ;

$$\text{laminer}: Re \leq 5 \times 10^5 \text{ , turbulent}: 5 \times 10^5 \leq Re \leq 10^7 \tag{2.5}$$

$$Re = \frac{1.225 \times 25 \times 0.275}{1.789 \times 10^{-5}} = 470758.804 \tag{2.6}$$

According to the calculated Reynolds number, the flow is turbulent. The boundary layer thickness is calculated in Eq. (2.7) and Eq. (2.8) Turbulence intensity is given in Eq's. (2.9)-(2.11). This turbulence intensity was used in the free entry of the flow;

$$\delta_L = \frac{0.37 \times c}{Re^{\frac{1}{5}}} \text{ (Total boundary layer thickness)} \tag{2.7}$$

$$\delta_L = \frac{0.37 \times 0.275}{470758.804^{\frac{1}{5}}} = 7.464 \times 10^{-3} \tag{2.8}$$

$I =$ turbulence intensity;

$$Re_g = \frac{\rho \times V \times \Delta h}{\mu} = \frac{1.225 \times 25 \times 1.5}{1.789 \times 10^{-5}} = 2567775.293 \tag{2.9}$$

$$I = 0.16 \times Re_g^{-\frac{1}{8}} = 0.16 \times 2567775.293^{-\frac{1}{8}} = 0.02529 \tag{2.10}$$

$$I = 2.529\% \tag{2.11}$$

The flow field is considered viscous, turbulent, and incompressible to exclude the solution of energy equations. The applicable equations for the current RANS (Reynolds-Averaged Navier-Stokes) calculations consist of the continuity equation and the momentum conservation equation, which are expressed as follows in Eq. (2.12) and Eq. (2.13): [27]
Continuity Equation;

$$\frac{\partial \rho}{\partial t} + \nabla(\rho \overrightarrow{u}) = 0 \tag{2.12}$$

Momentum Equation;

$$\frac{\partial (\rho \overrightarrow{u})}{\partial t} + \nabla(\rho \overrightarrow{u} \overrightarrow{u}) = \nabla(\mu \nabla \overrightarrow{u}) - \nabla p + \rho \overrightarrow{g} \tag{2.13}$$

Here, $\overrightarrow{u}$ denotes the velocity vector in the x, y and z directions, p denotes the pressure, μ denotes the dynamic viscosity, and ρ denotes the fluid density.
It was decided to use the $k-\omega$ sst turbulence model equation (2.4) (2.5) due to its ability to accurately model adhesion loss and flow separation of airfoils among the results stated in the literature [28]. The grid structure of the model to be used in flow analysis is important. In 2D wing examinations, the total thickness parameter on the wing was modelled as a grid with 25 layers based on the result shown by the mesh (grid) program (first model) and the results were obtained. Lift and drag coefficients are shown in Table 2.2. After obtaining the results with the first model, the results were obtained by creating layers (final model) with the first layer by taking $y = +1$ and increasing by 35 layers. The latest model structure was used in the investigations.

$$\begin{aligned}
\frac{\partial(\rho k)}{\partial t} + div(\rho k U_i) &= div\left[\left(\mu + \frac{pk}{\omega\sigma_k}\right)\nabla k\right] + 2\frac{(\rho k)}{\omega} S_{ij}.S_{ij} - \frac{2}{3}\rho k \frac{\partial U_i}{\partial x_j} S_{ij} - \beta * \rho k w \\
\frac{\partial(\rho\omega)}{\partial t} + div(\rho\omega U_i) &= div\left[\left(\mu + \frac{\rho k}{\omega\sigma_{\omega^1}}\right)\nabla\omega\right] + 2\rho\gamma_2 S_{ij}.S_{ij} - \frac{2}{3}p\gamma_2\omega\frac{\partial U_i}{\partial x_j} S_{ij} - \beta_2\rho\omega^2 + 2\frac{\rho}{\omega\sigma_{\omega^2}}\frac{\partial k}{\partial x_k}\frac{\partial\omega}{\partial k_k}
\end{aligned}$$

Table 2.2: C_l and C_d values at different angles of attack in 2D analysis

	First model (initial)			Last model (stable)		
AoA	C_l	C_d	C_l/C_d	C_l	C_d	C_l/C_d
0	0.449	0.0227	19.756	0.466	0.0174	26.698
2	0.670	0.1819	36.842	0.695	0.0193	36.024
5	0.960	0.0227	42.227	1.004	0.0239	31.861
10	1.331	0.0378	35.148	1.381	0.0390	35.350
12	1.412	0.0488	28.920	1.462	0.0500	29.233
13	1.426	0.0560	25.440	1.495	0.0579	26.826
14	1.419	0.0658	21.560	1.504	0.0681	22.078
15	1.395	0.0808	17.262	1.483	0.0823	18.019

2.2. Model verification

The effect of the number of elements was examined for 3D numerical models used in examining wing structures. Drag and lift coefficients, which are a result of aerodynamic effects, were used as the basis for validation. 3 different wing designs were investigated. In Table 2.3, C_l and C_d results of numerical analyses were given.

Table 2.3: C_l and C_d values in different wings according to the number of elements

Wing type	Number of elements	C_l	C_d	C_l/C_d
rectangular	5007723	0.3259	0.0208	15.667
	2286244	0.3496	0.2126	16.443
	1307221	0.3605	0.0214	16.773
	870499	0.3656	0.0217	16.842
trapezoidal	5074373	0.3308	0.02064	16.025
arrow-angle	9361220	0.2975	0.01976	15.055
	6241939	0.31405	0.0201158	15.612
	5178034	0.31462	0.0201492	15.612
	5186810	0.32481	0.0207111	15.683
	2348390	0.33392	0.0204356	16.340
	1341935	0.34584	0.0206863	16.718
	965296	0.35246	0.0209365	16.835

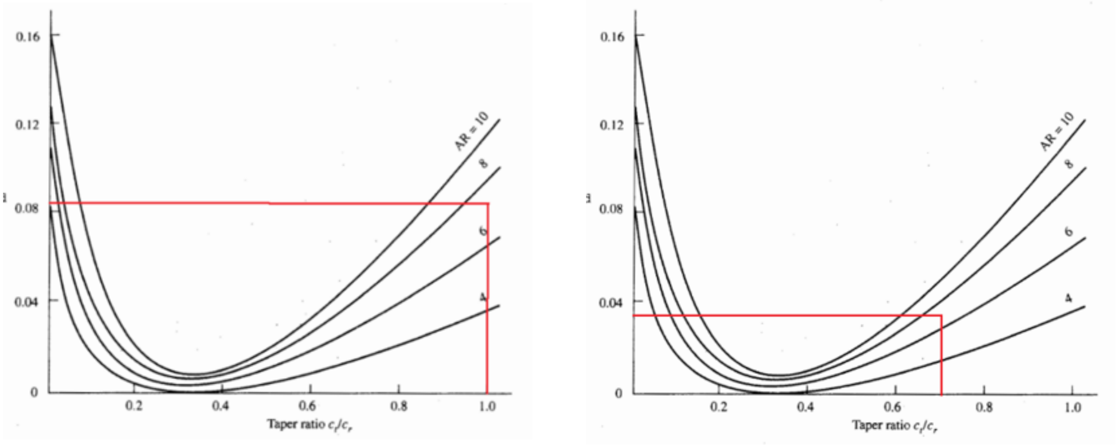

(a) **(b)**

Figure 2.3: Induced drag factor, δ(a: rectangular; b: trapezoidal)

2.2.1. Rectangular wing lift coefficient verification

At the outset of the 3D model analysis, the quantity of elements was analyzed for considering the lift coefficient (C_l) and drag coefficient (C_d) of the rectangular wing. The findings are summarized in Table 3. It was determined that stable results were achieved using the highest element number from the table, and subsequent examinations were conducted at this element density. The maximum value was then considered the optimal mesh and compared to the theoretical lift coefficient (C_l) value. Induced drag factor was taken from Figure 2.3a for a taper ratio of 1 and AR was 7.27; $\delta = 0.083$.

$$
\begin{aligned}
a &= \frac{dC_L}{d\alpha} \\
a &= \frac{a_0}{1+\frac{a_0}{\pi \times e \times AR}} \\
e &= \frac{1}{1+\delta} = \frac{1}{1+0.083} = 0.92336 \\
\delta &\cong 0.083\,(\text{Induced drag factor}) \\
a &= \frac{6.02}{1+\frac{6.02}{\pi \times 0.92336 \times 7.27}} = 4.68315\,\text{radian} \\
a &= \frac{4.68915}{57.3} = 0.08173 \text{ deg} \\
C_L &= a \times (\alpha - \alpha_{L=0}) = 0.08173 \times (0-(-4)) = 0.326921 \\
\text{Error ratio} &= \frac{\left|C_{L\,analy.} - C_{L\,real}\right|}{C_{L\,real}} \times 100 = \frac{|0.329121-0.326921|}{0.326921} \times 100 = 0.67\%
\end{aligned}
$$

Here, the first α in parentheses is 0°, which is the angle of the wing. $\alpha_L = 0$ is the angle of attack at which the airfoil is at zero lift.

2.2.2. Trapezoidal wing lift coefficient verification

The error ratio was calculated for trapezoidal wing and was given in Eq. 27. δ was taken from Figure 2.3b. The taper ratio was $225\,mm/325\,mm = 0.6923$ which was shown previously in Figure 2.2. $AR = 7.27$ and δ is obtained 0.035.

$$
\begin{aligned}
a &= \frac{dC_L}{d\alpha} \\
a &= \frac{a_0}{1+\frac{a_0}{\pi \times e \times AR}} \\
\delta &\cong 0.035\,(\text{Induced drag factor}) \\
e &= \frac{1}{1+\delta} = \frac{1}{1+0.035} = 0.966183 \\
a &= \frac{6.02}{1+\frac{6.02}{\pi \times 0.966183 \times 7.27}} = 4.729711\,\text{radian}\frac{n!}{r!\,(n-r)!} \\
a &= \frac{4.729711}{57.3} = 0.0825429\,deg \\
C_L &= a \times (\alpha - \alpha_{L=0}) = 0.082635 \times (0-(-4)) = 0.330171 \\
\text{Error ratio} &= \frac{\left|C_{L\,analy.} - C_{L\,real}\right|}{C_{L\,real}} \times 100 = \frac{|0.333242-0.330171|}{0.330171} \times 100 = 0.93\%
\end{aligned}
$$

2.2.3. Arrow angle wing list coefficient verification

Arrow-angle wing lift coefficient was calculated for a 25° back arrow angle.

$$
\begin{aligned}
a &= \frac{dC_L}{d\alpha} \\
\cos(\wedge) &= \cos(25)\,(back\,arrow\,angle) \\
a &= \frac{a_0 \times \cos(\wedge)}{\sqrt{1+\left(\frac{a_0 \times \cos(\wedge)}{\pi \times AR}\right)^2} + \frac{a_0 \times \cos(\wedge)}{\pi \times AR}} \\
a &= \frac{6.02 \times \cos(25)}{\sqrt{1+\left(\frac{6.02 \times \cos(25)}{\pi \times 7.27}\right)^2} + \frac{6.02 \times \cos(25)}{\pi \times 7.27}} = 4.306509\,radian \\
a &= \frac{4.306509}{57.3} = 0.07515\,deg \\
C_L &= a \times (\alpha - \alpha_{L=0}) = 0.07515 \times (0-(-4)) = 0.3006 \\
\text{Error ratio} &= \frac{\left|C_{L\,analy.} - C_{L\,real}\right|}{C_{L\,real}} \times 100 = \frac{|0.297495-0.3006|}{0.3006} \times 100 = 1.033\%
\end{aligned}
$$

Error rates were deemed to be acceptable, and investigations continued.

3. Results and Discussion

3.1. Lift and drag coefficients on wings

Subsequent to juxtaposing the theoretical predictions with the empirical findings, varying angles of attack influenced the lift (C_l) and drag (C_d) coefficients were explored. The C_l, C_d and C_l/C_d results were given in Tables 3.1, 3.2 and 3.3 for rectangular, trapezoidal and arrow-angle wing, respectively. Upon analysis of the lift coefficient, it was observed that for all models, the lift coefficient escalated with the angle of attack (AoA) up to 15°. Notably, the trapezoidal wing exhibited the most substantial lift coefficient. In contrast, the rectangular wing demonstrated lift coefficients comparable to the trapezoidal wing, yet its lift coefficient ceased to rise beyond an AoA of 12°. Beyond an angle of attack (AoA) of 15°, both the rectangular and trapezoidal wings experienced a decline in their lift coefficients. Conversely, the arrow-angle wing model, despite having a lower lift coefficient initially, continued to see an increase in its lift coefficient until reaching an AoA of 20°.

As for the drag coefficient, the drag coefficient of all wing models increases with increasing AoA. Rectangular and trapezoidal wings gave similar results, while arrow-angle wing showed lower drag coefficient. For all models, the ratio of lift coefficient to drag coefficient (C_l/C_d) rises until reaching an angle of attack of 5°. Beyond this angle, the ratio begins to decline. The lift-to-drag ratio (C_l/C_d) for the trapezoidal wing model surpassed others until an angle of attack of 14°, whereas the arrow-angle wing model's lift-to-drag ratio peaked at angles of attack exceeding 14°.

Table 3.1: Rectangular wing cl and cd values according to angles of attack

AoA (°)	C_l	C_d	C_l/C_d
0	0.32912137	0.020896613	15.74998637
5	0.73337471	0.037799812	19.40154385
10	1.0710421	0.069095768	15.50083501
12	1.1446231	0.088171176	12.98182866
14	1.1431234	0.11931991	9.580324021
15	1.1657	0.13733	8.488312823
16	1.1204377	0.15640722	7.163593215

Table 3.2: Trapezoidal wing C_l and C_d values according to angles of attack

AoA (°)	C_l	C_d	C_l/C_d
0	0.32912137	0.020896613	15.74998637
5	0.73337471	0.037799812	19.40154385
10	1.0710421	0.069095768	15.50083501
12	1.1446231	0.088171176	12.98182866
14	1.1431234	0.11931991	9.580324021
15	1.1657	0.13733	8.488312823
16	1.1204377	0.15640722	7.163593215

Table 3.3: Arrow-angle wing C_l and C_d values according to angle of attack

AoA (°)	C_l	C_d	C_l/C_d
0	0.29749516	0.01976	15.055423
5	0.67764535	0.03507	19.321561
10	0.999483325	0.06286	15.825955
12	1.0812807	0.07832	13.80603
14	1.1373059	0.09892	11.496681
15	1.1560672	0.11254	10.272294
17	1.1951	0.14812	8.068458
18	1.2143577	0.17092	7.1047906
19	1.2318	0.19423	6.3419657
20	1.23	0.22149	5.5532981

3.2. Pressure contours formed on wings

Imaging the flow around a wing is complex, and pressure contours are widely used to express this interaction. The effects of different angles of attack are compared for rectangular, trapezoidal and arrow-angle wing models and are shown in Figures 3.3, 3.4 and 3.5. Based on the side view of the wings, a plane was created at a distance 0.5 m from the wing-fuselage junction and the pressure contours formed in this plane are shown. Results up to 16° angle of attack on rectangular and trapezoidal wings and up to 18° angle of attack on arrow-angle wings are shown and compared with each other. For the values shown by the contours, the highest positive pressure is labelled with the letters H++ (red colour), the intermediate pressure is labelled with the letters H+ (orange) and H (yellow). In negative pressures, the highest value is labelled with the letters L– (dark blue), medium pressure L- (light blue) and low-pressure L (green). It was observed that at 0° angle of attack, there was a negative low pressure (L) on the upper surface of all wings and a low positive pressure under the wings. There was the highest positive pressure at the front end of the wing due to the edge that interacts the flow. While the highest pressure occurred at the H++ level in the rectangular and trapezoidal wing structure, it occurred at the H+ level in the arrow-angle wing. It can be said that the sweep angle effect in the arrow-angle wing provides less pressure formation at the wing tip. It was observed that a negative low pressure (L) occurred at the bottom of the leading edge of the wings. NACA 4412 airfoil is not fully symmetrical. The fact that the underside of the wing is less humped than the top of the wing ensured the formation of this low pressure after the separation of the flow at the wing tip.

For the trapezoidal wing, the outcome at a 2° angle of attack indicated the clear formation of an L- pressure on the wing's surface. The pressure at the tip of the wing has intensified, leading to a significant increase in H++ pressure. However, this high-pressure area has become smaller and is now mostly confined to the wing's tip. When analysing the impact at a 5° angle of attack, it's observed that the pressure patterns on both rectangular and trapezoidal wings are quite alike. With an increase in the wing's angle of attack, the zone of maximum pressure, denoted as H++, has moved a bit from the center of the wing's tip towards the wing's underside. All wings have developed a negative medium pressure, labelled as L-. Nonetheless, the positive pressure beneath the wing isn't substantial. In contrast to other wing shapes, the arrow-angle wing doesn't exhibit the highest pressure, H++, at its front edge.

At 10° angle of attack, the teardrop aerofoil's lift became more pronounced. The peak positive pressure shifted from the wing's tip to its underside and the high-pressure zone, H+ enlarged. Meanwhile, the wing's negative pressure regions also increased. The arrow-angle wing did not experience the highest pressure, H++, and the negative pressure area, L–, was smaller and located in front of the wing's upper chamber. When the angle increased to 12°, the separation of pressure at the wing's front edge was noticeable, with positive pressure at H level. Both L– and H+ pressure areas got bigger. The negative pressure, L, extended over the wing's top surface to its back end. The L zone was most extensive on rectangular wings and smallest on arrow-angle wings. At 14° AoA, the trapezoidal wing predominantly showed high pressure underneath and low-pressure variations on top. The negative pressure region, L, expanded across all wing types. The area with the utmost positive pressure, H++, remained the same on rectangular and trapezoidal wings but reduced on the arrow-angle wing.

The airflow patterns around the wings changed noticeably at a 15° angle of attack. For rectangular and trapezoidal wings, the negative pressure zones above the wing decreased, whereas they increased for the arrow-angle wing. This trend continued at 16°. At 17 and 18°, only results for the arrow-angle wing were observed. Despite increasing angles of attack, the negative pressure on the wing developed and expanded smoothly. The positive pressure distribution underneath the wing remained unaffected.

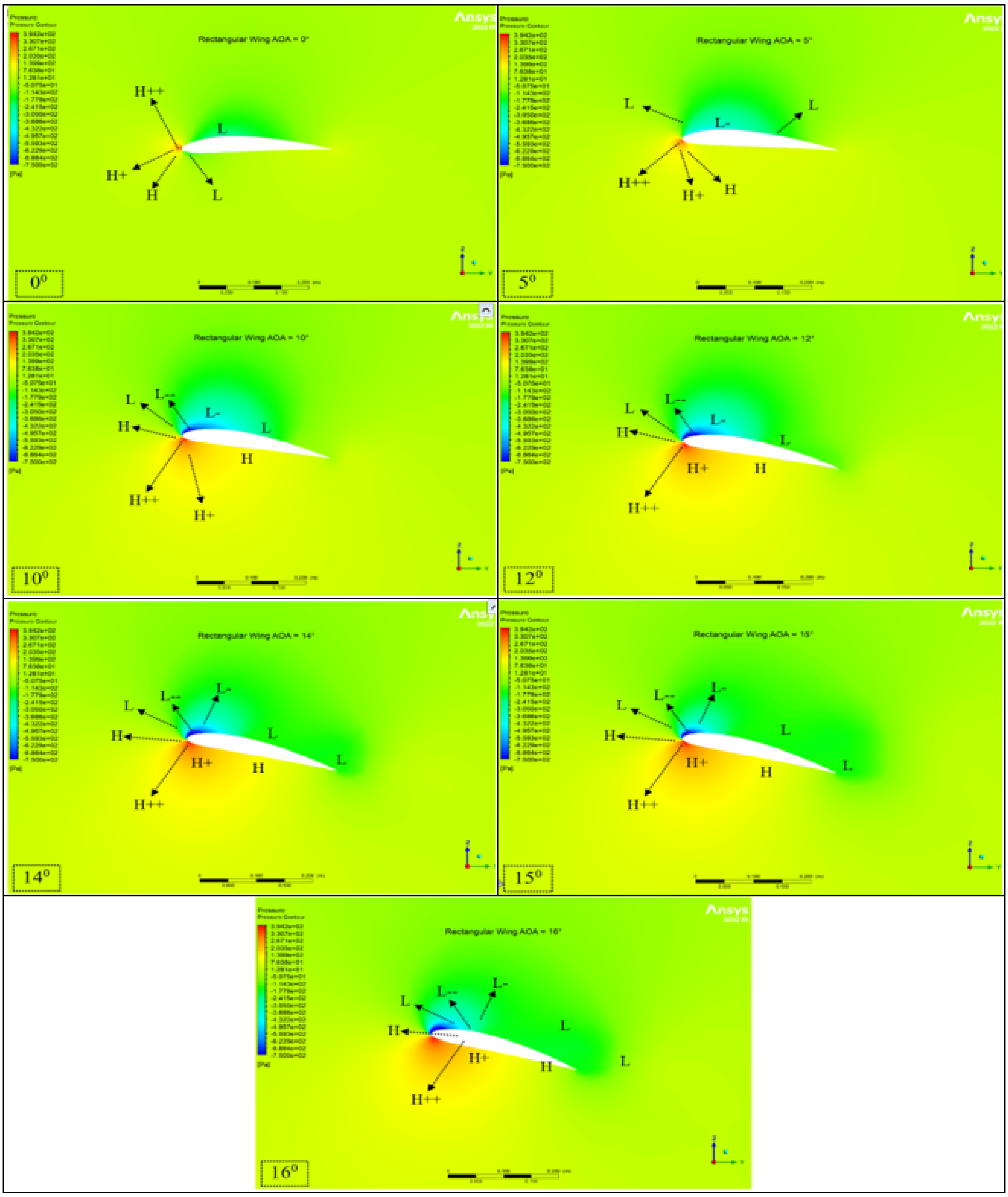

Figure 3.1: Pressure distributions of rectangular wing at $0-5-10-12-14-15-16^{\circ}$ of angles of attack

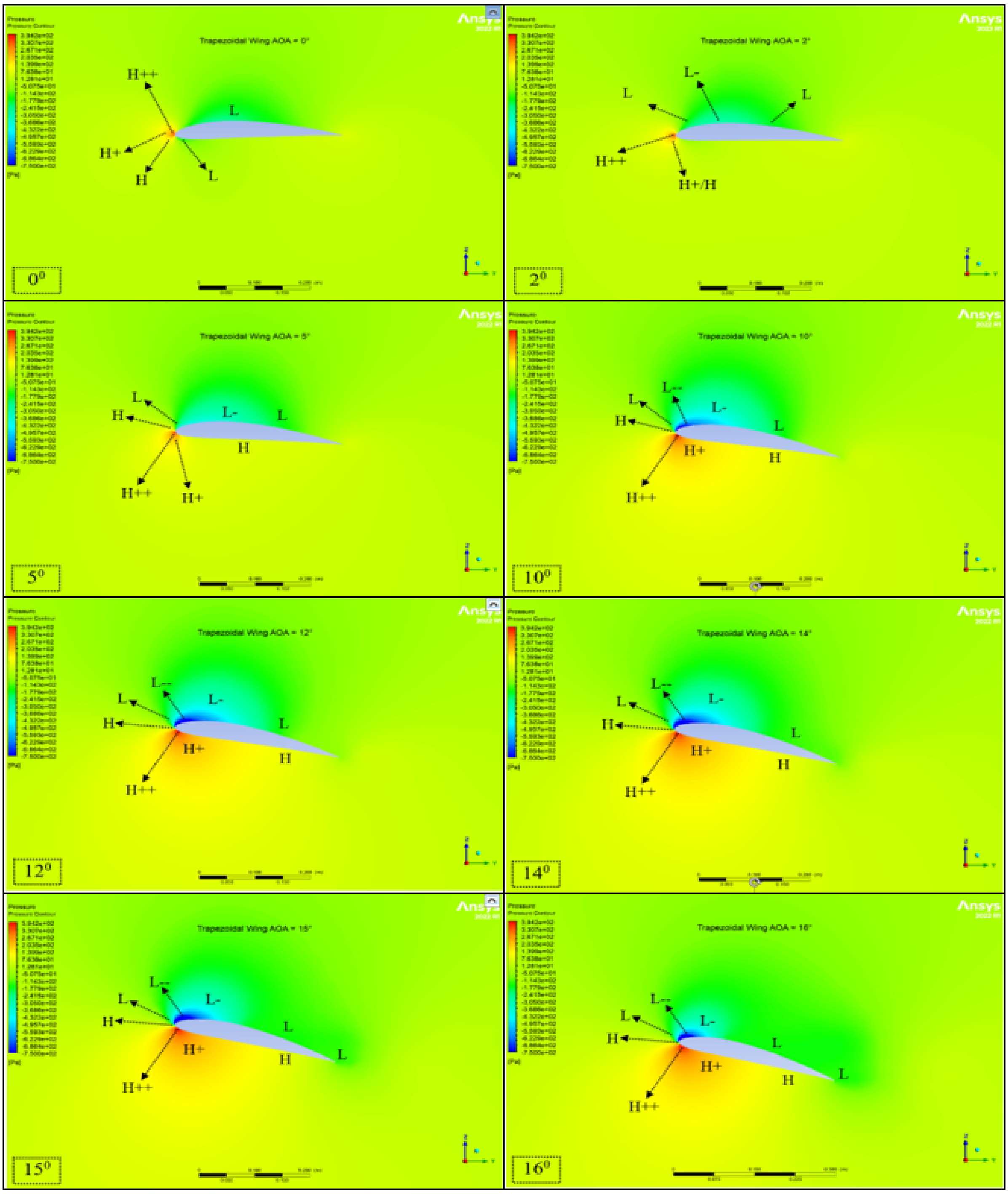

Figure 3.2: Pressure distributions of trapezoidal Wing at $0-2-5-10-12-14-15-16^\circ$ of Angles of Attack

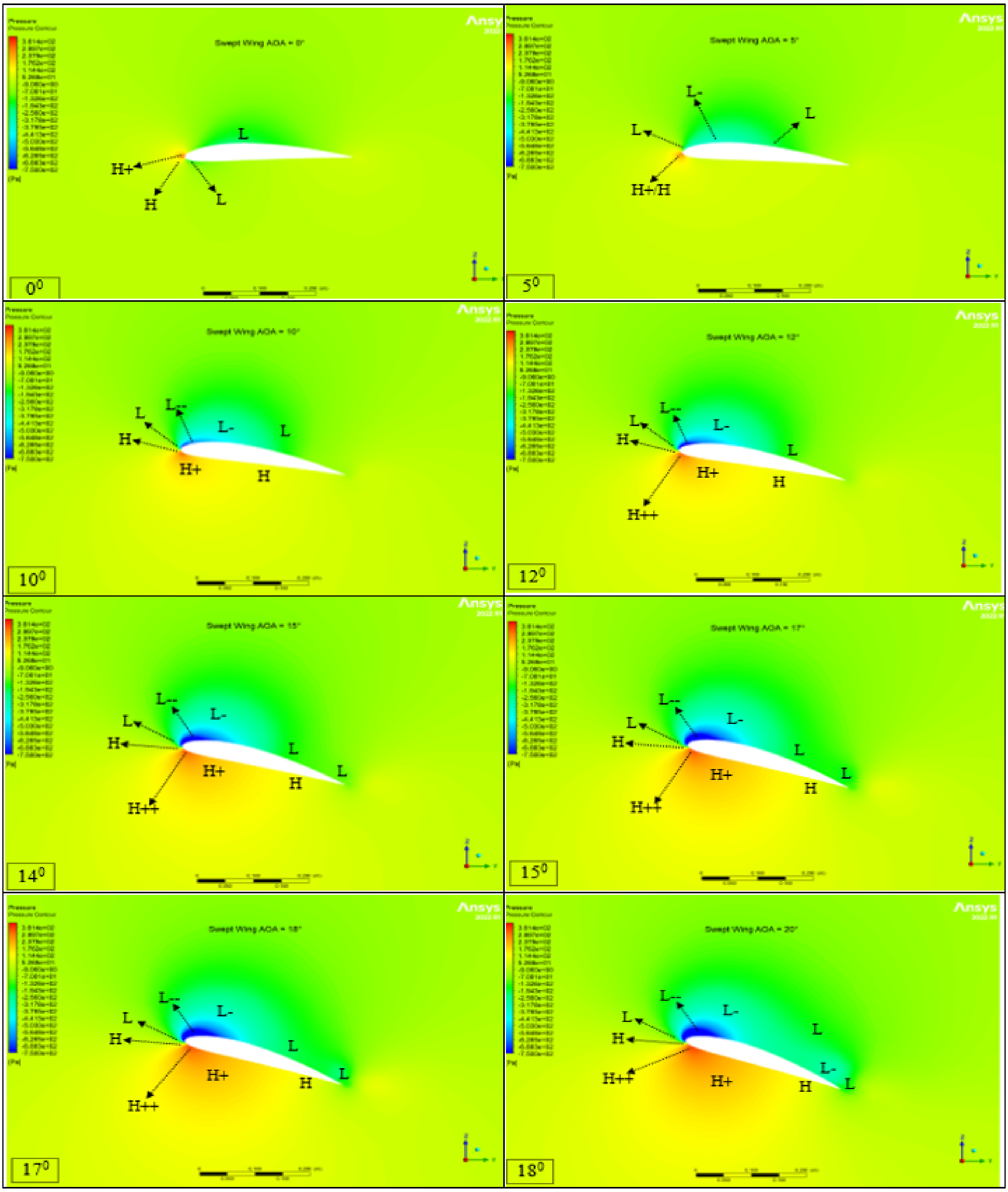

Figure 3.3: Pressure distributions of arrow angle wing at 0 – 5 – 10 – 12 – 14 – 15 – 17 – 18° of angles of attack

3.3. Velocity contours around wings

The velocity contours formed around the wings are shown in Figures 3.4, 3.5 and 3.6 for rectangular, trapezoidal and arrow-angle wings. Based on a free flow speed of 25 m/s, regions of low-speed formation were identified near the leading edge and behind the wing. Due to the teardrop wing profile structure, the flow velocity increased on the upper surface of the wing. Furthermore, there's an observable increase in flow velocity within a specific area along the bottom of the wing's leading edge. The formation of low pressure with increasing velocity becomes more evident when comparing speed and pressure contours simultaneously. At tha 2° angle of attack, the high-speed region beneath the trapezoidal wing decreased. Increasing the angle of attack to 5° led to an expansion of the high-speed area on the wing, particularly noticeable in the trapezoidal and arrow-angle wing designs. As the flow speed increases over the upper surface of the trapezoidal wing, separation of flow from the wing surface begins to occur at the rear of the wing camber.

At a 10° angle of attack, an SP was noted on all three types of wings. With an increase in the angle of attack, the low-velocity profile, which appears as a wake trailing the wing, extended from the rear of the wing to its upper side. In the arrow-angle wing, the low velocity profile on the wing covers a smaller area. When the angle of attack is set to 12°, the wing tips experience the highest velocity, while simultaneously, a region of lower velocity is created just beneath the wing tips because of the wings separating the airflow. At 14° angle of attack, the velocity variations across different wing shapes are noticeable. For the rectangular wing, the stagnation point is at the wing's camber peak, creating a broad zone of reduced the velocity behind it. The trapezoidal wing has a smaller area of low velocity on its surface. Yet, the most pronounced effect is the increased velocity at the wing's leading edge. With the arrow-angle wing, the stagnation point is found towards the back, resulting in a sparse area of low velocity. The extensive low-velocity profile generated by a 15° rectangular wing behind it covers a large area, which is not conducive for optimal wing performance. In the trapezoidal wing, the low-velocity region has expanded, and the separation point has shifted towards the wing's leading edge. However, there was no alteration observed in the profile of the arrow-angle wing. At a 16° angle of attack, overwing flow disruption occurs in the trapezoidal wing. For arrow-angle wings at attack angles of 17° and 18°, it's observed that there's a significant area of low velocity beneath the wing. At an 18° angle of attack, the airflow is noted to create a reverse flow pattern in the low velocity region above the wing.

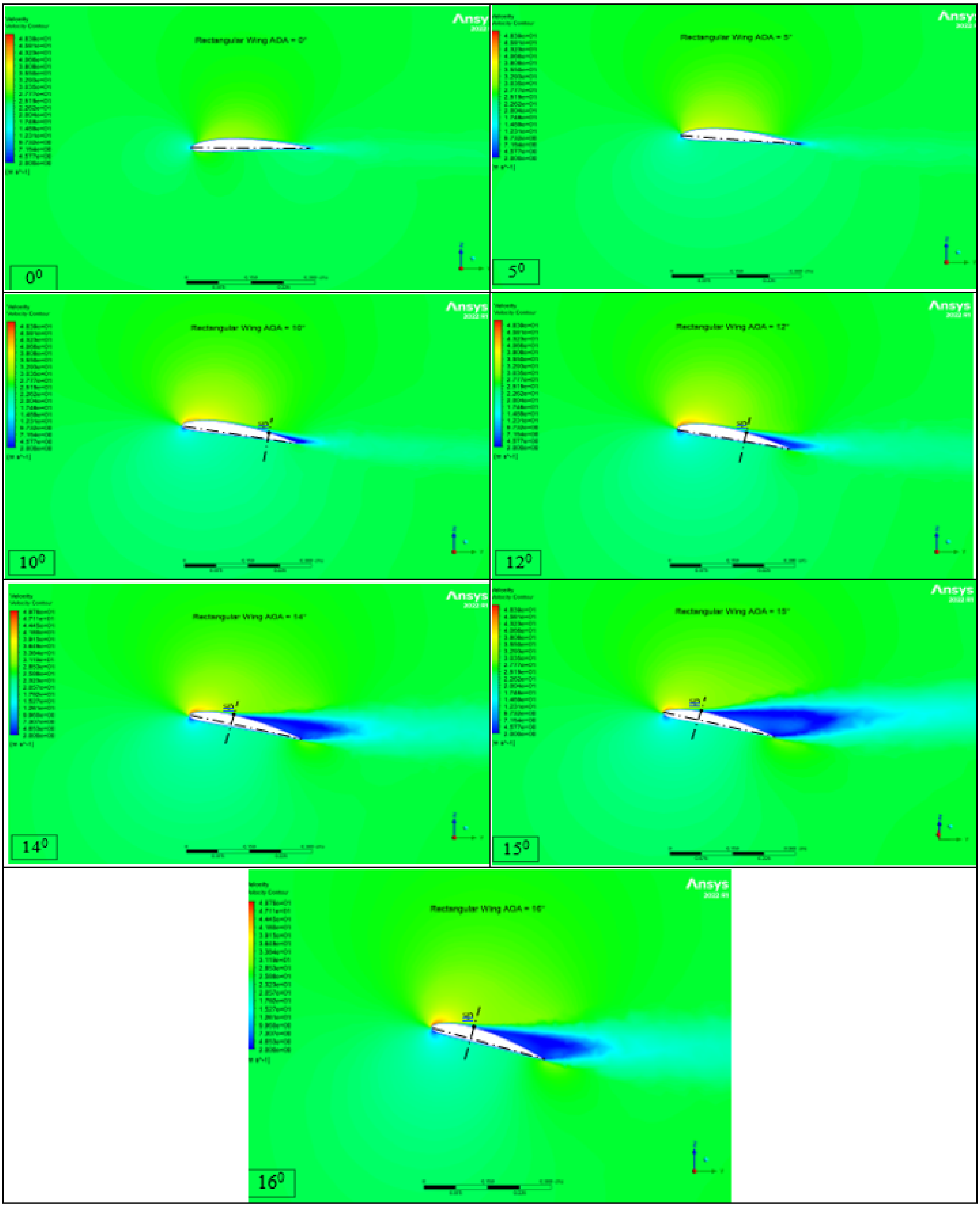

Figure 3.4: Velocity contours of rectangular wing at $0-5-10-12-14-15-16^{\circ}$ of angles of attack

3.4. Vortices around wings

Prominent vortex patterns around the wing and along the direction of airflow were illustrated in Figures 3.7, 3.8 and 3.9. Interactions between the flow and the wing resulted in the wing being enveloped by numerous small vortices. Notably, there's an absence of vortex development at the wing's trailing edge, where the airflow is disrupted by the wing structure. Vortex generation at the wingtips occurred at every angle of attack. For a rectangular wing, the wingtip vortex significantly affects the surrounding area once the angle of attack exceeds 5°. The trapezoidal wing exhibits the least amount of wingtip vortex. As the angle of attack increases, the vortices on the wing's upper surface become more chaotic, leading to their detachment from the wing's surface sooner, before they can reach the wing's rear. At attack angles

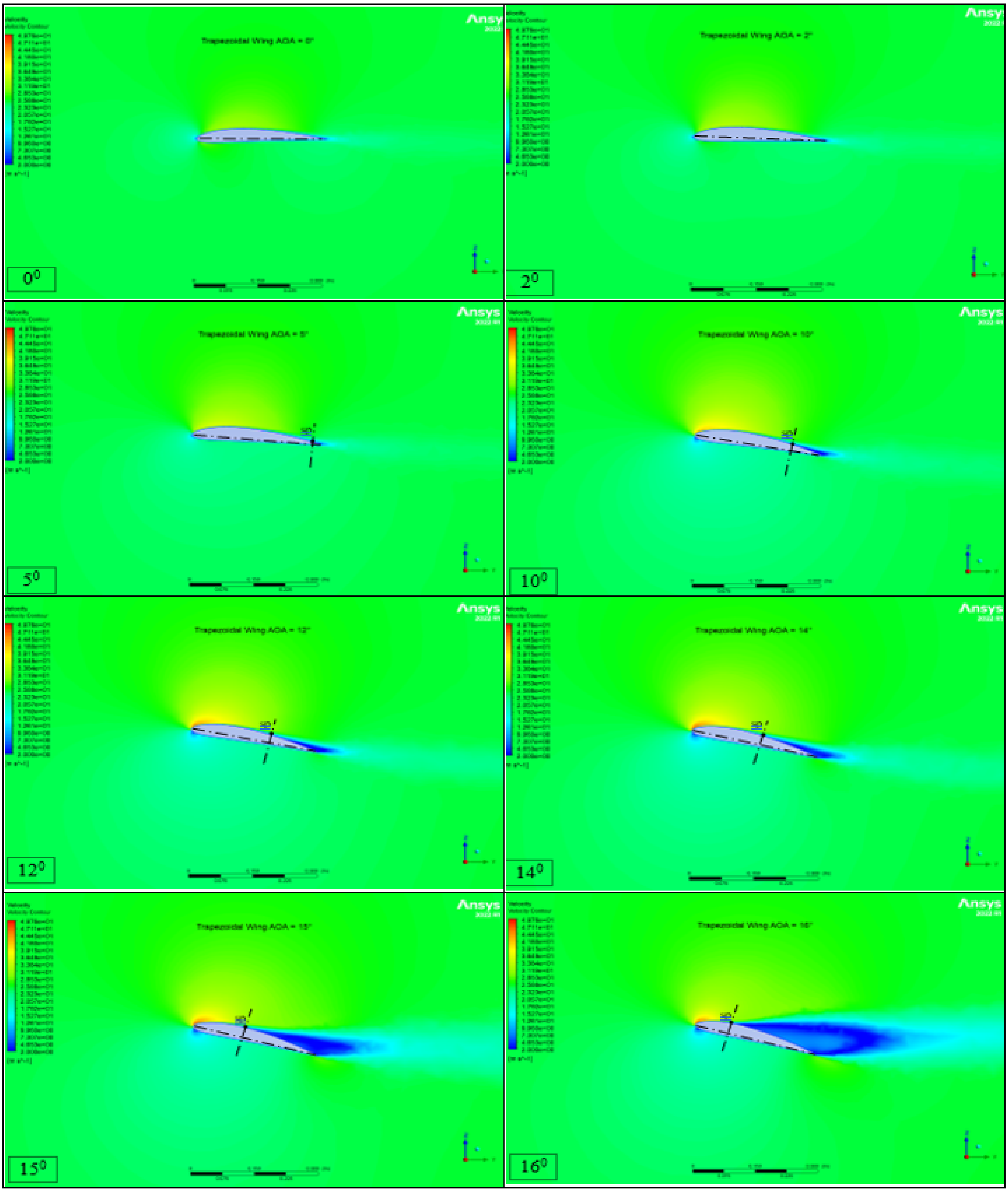

Figure 3.5: Velocity contours of trapezoidal wing at $0-2-5-10-12-14-15-16°$ of angles of attack

of 0, 2, and 5°, the wing surface vortices were formed in a stable manner. When the angle of attack reached 10°, there were noticeable disturbances in the flow along the entire length of the wing, particularly at the trailing edge. At an angle of attack of 12°, the rectangular wing's surface showed minor disruptions due to vortex merging, a phenomenon not yet seen on trapezoidal and arrow-angle wings. At 14°, the minor disturbances on the rectangular wing's surface became more pronounced. The trapezoidal wing began to exhibit small to medium-sized vortex disruptions, and the arrow-angle wing started to show small-scale vortex disturbances. At 15° angle of attack, the rectangular wing experienced the formation of a significant vortex, while the trapezoidal wing had two vortices of medium size, and the arrow-angle wing developed small to medium vortices spread across its surface. For the rectangular and trapezoidal wings at a 16° angle of attack, large vortices were present on the wing surfaces, which substantially disrupted and destabilized the airflow. However, on the arrow-angle wing at attack angles of 17° and 18°, the flow irregularity was minimized near the junction of the wing and the *UAV* body. Conversely, on the other wing types, the connection point to the fuselage showed increased irregularity and larger vortex formations.

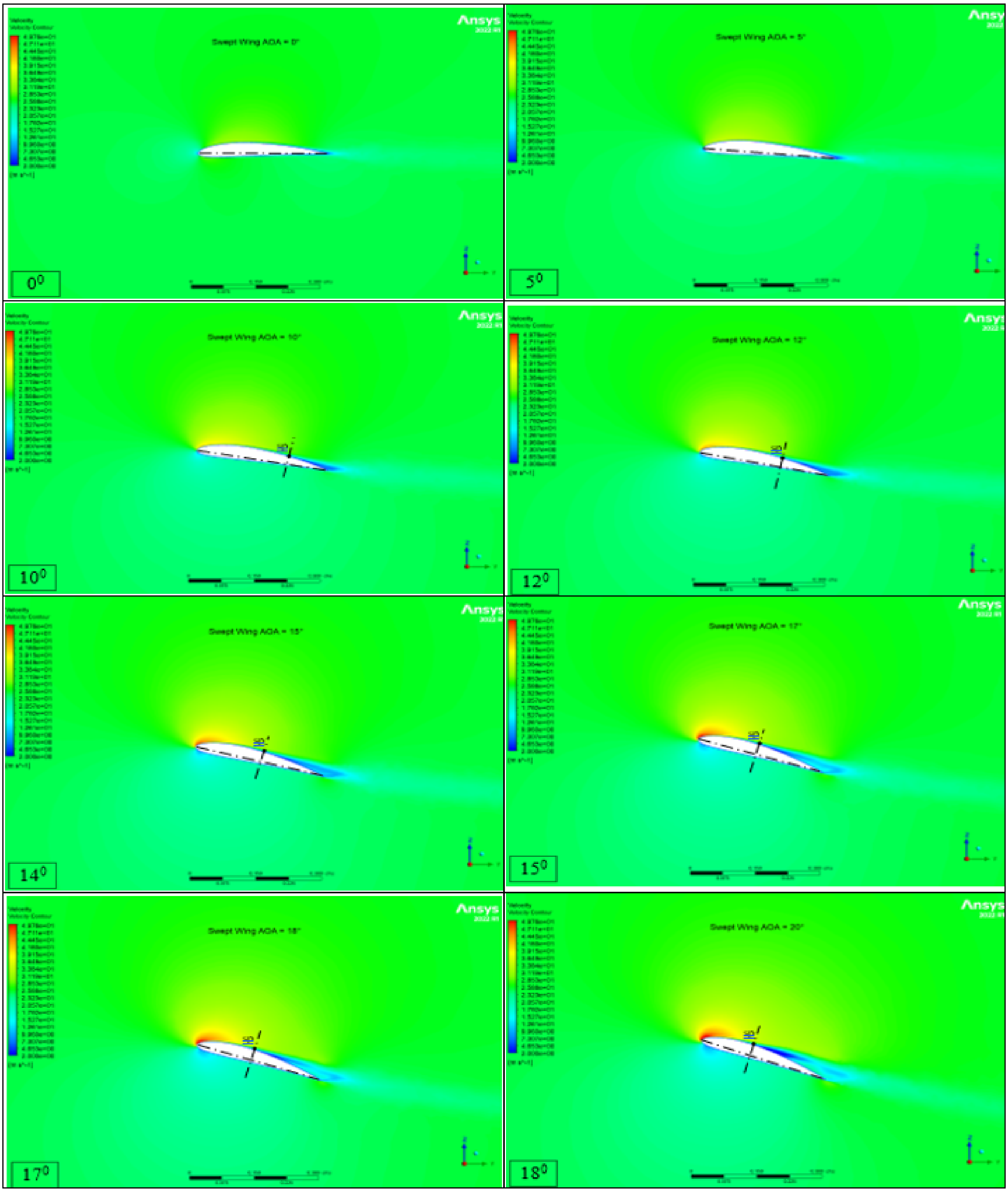

Figure 3.6: Velocity contours of arrow angle wing at $0-5-10-12-14-15-17-18^\circ$ of angles of attack

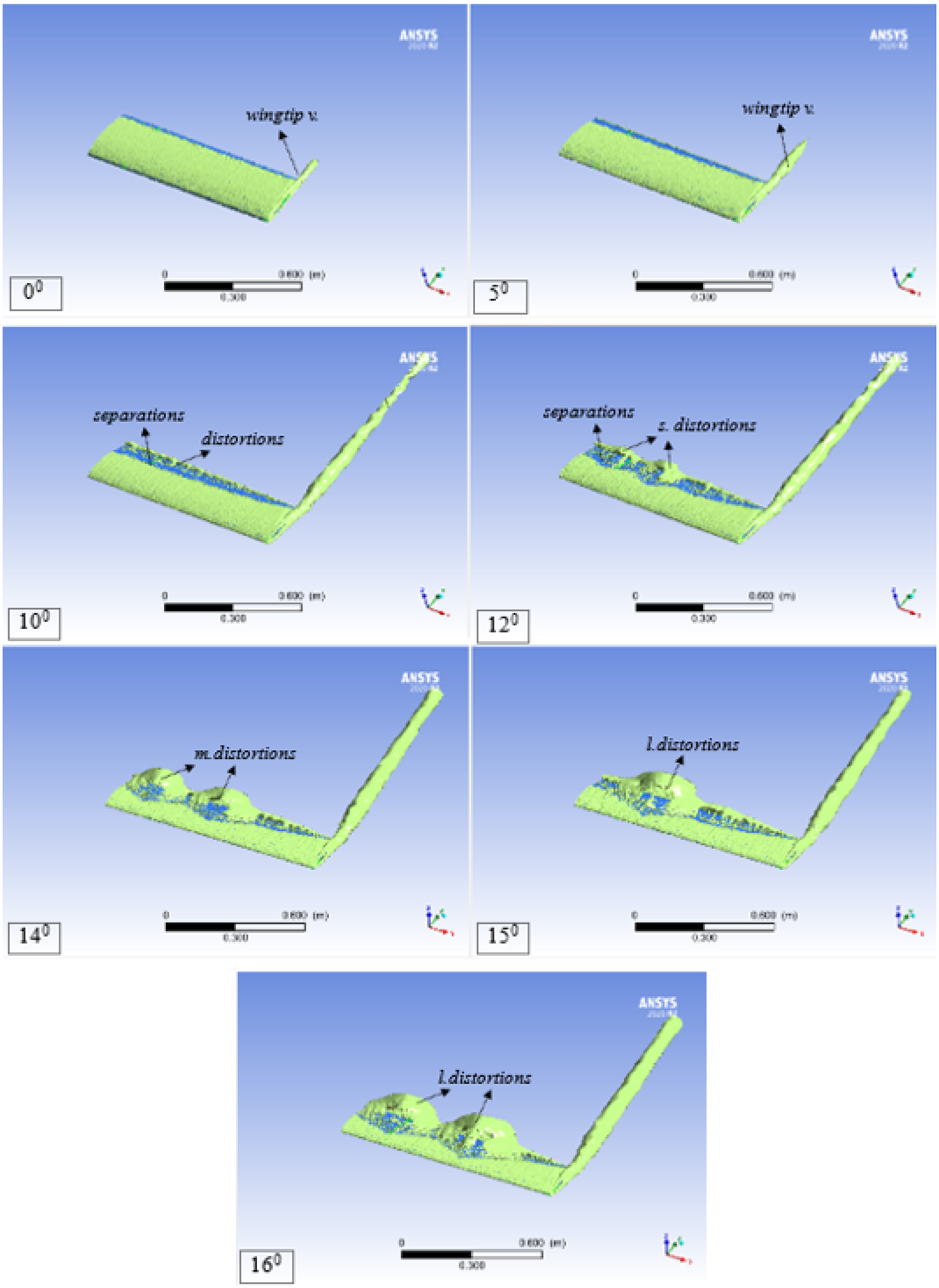

Figure 3.7: Vortex formations of rectangular wing at $0-5-10-12-14-15-16^\circ$ of angles of attack

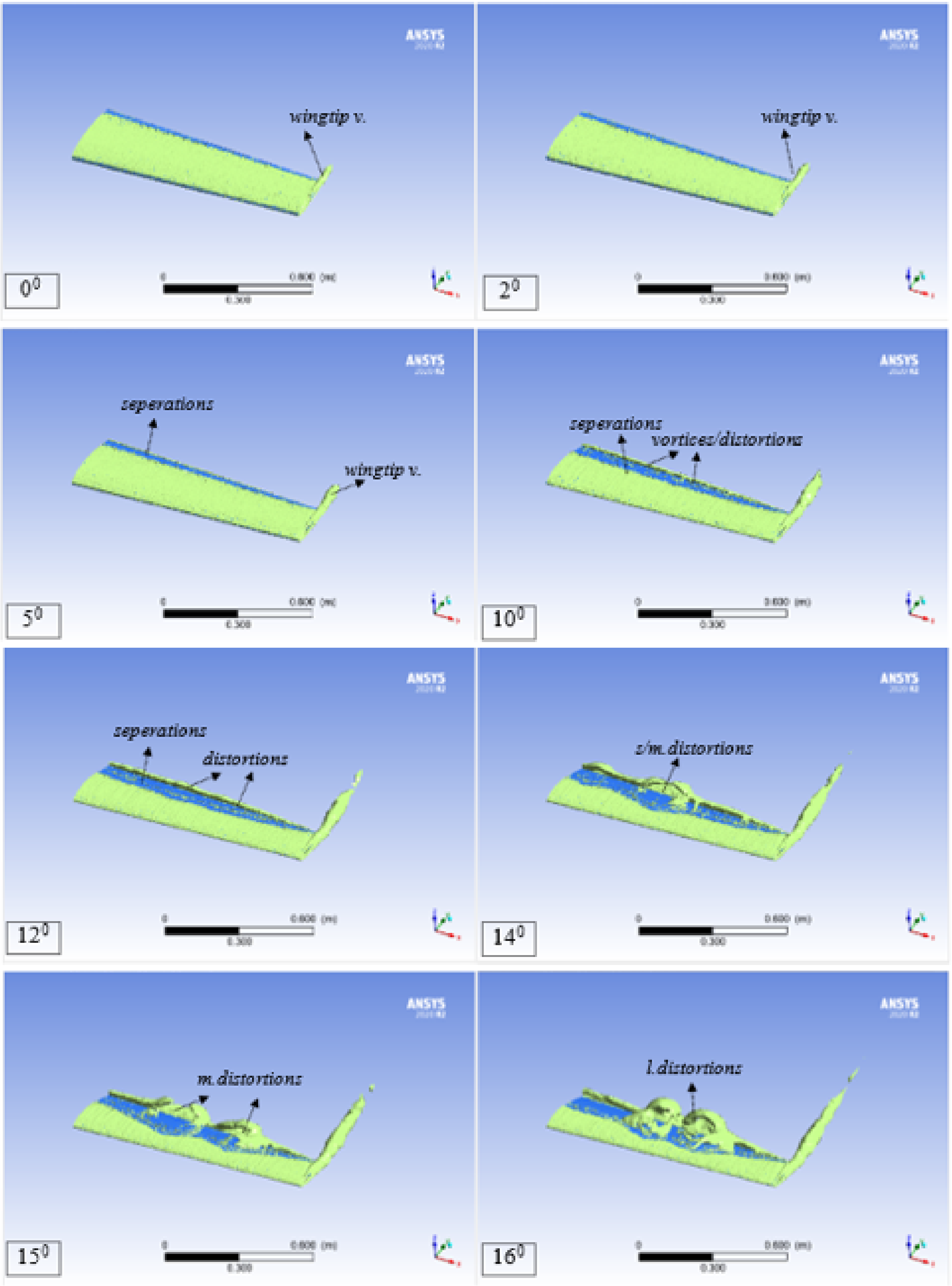

Figure 3.8: Vortex formations of trapezoidal wing at $0-2-5-10-12-14-15-16^\circ$ of angles of attack

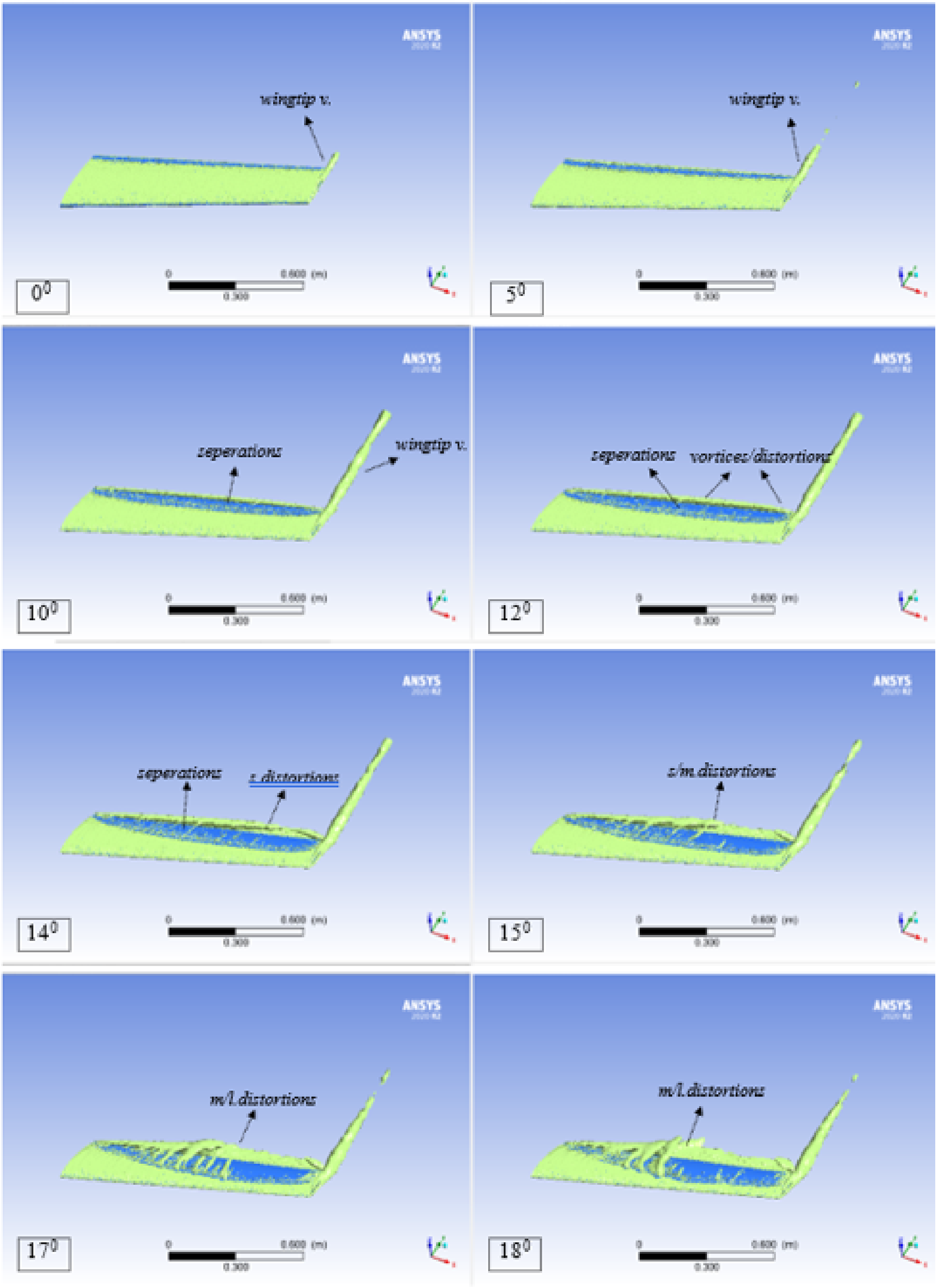

Figure 3.9: Vortex formations of arrow angle wing at 0 – 5 – 10 – 12 – 14 – 15 – 17 – 18° of angles of attack

3.5. Pressure behaviour of the body and tail wing

Flow analysis conducted on the body revealed that it generates a slight lift. The lift coefficient (C_l) and drag coefficient (C_d) were found to be 0.00015200737 and 0.0084482443, respectively. Figure 3.10 illustrates the pressure contours for the body alone. The body's basic cylindrical shape and the tapered design at both ends ensure even pressure distribution on and around the body, with minimal pressure variation. Consequently, the wings are responsible for generating the necessary lift force. The maximum pressure was observed at the front part of the body, specifically at the nose of the fuselage.

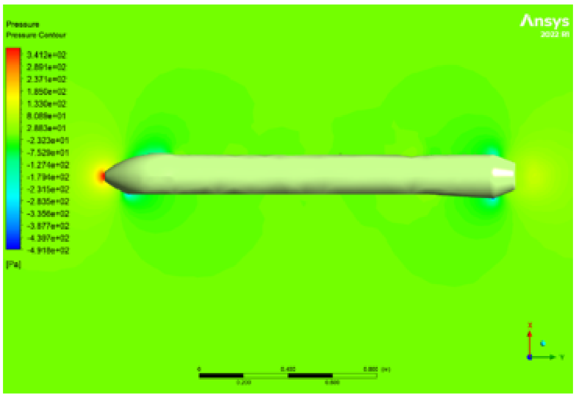

Figure 3.10: Pressure contours from the middle of fuselage

Figure 3.11 depicts the tail wings, which are designed with a distinct drop section model compared to the main wings. The profile's geometry results in high pressure exclusively at the front wing's leading edges where the airflow first impacts. The rest of the wing and its trailing edges experience a consistent pressure distribution. The V-shaped tail is confirmed to produce a measurable lift effect.

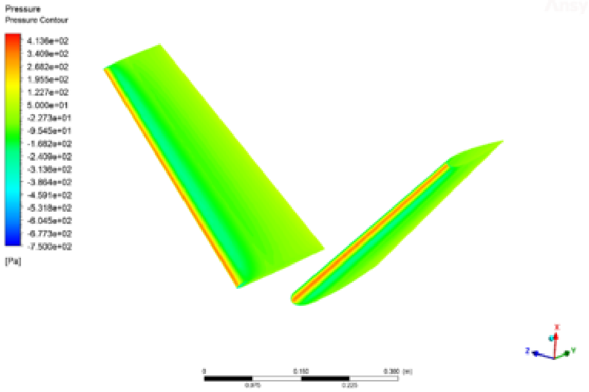

Figure 3.11: Tail pressure distribution

3.6. Effect of wing layout on lift and drag

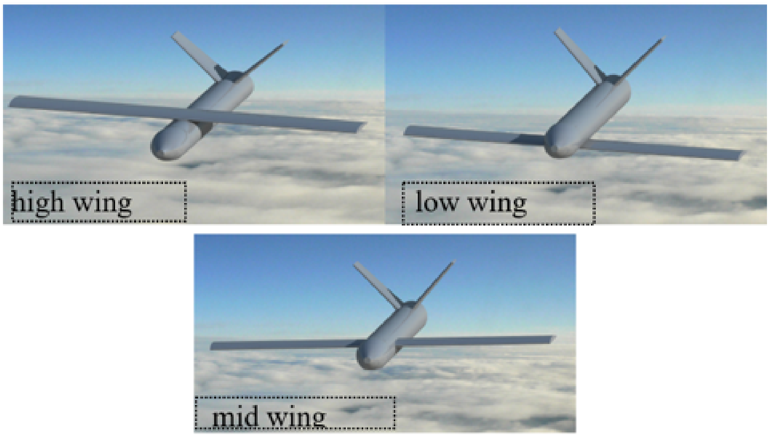

Figure 3.12: Location of the wing on the fuselage

The point where the wings attach to the main body, or fuselage, is crucial. Figure 3.12 displays three different wing attachment locations: high, mid, and low. Table 3.4 lists the lift (C_l) and drag (C_d) coefficients resulting from these wing-fuselage configurations. The arrow-angle from below model showed the highest lift coefficient, while the trapezoidal from the middle model had the best C_l/C_d ratio. Thus, the trapezoidal middle model is the preferred choice. Based on this, Figure 3.13 presents the pressure outcomes for rectangular, trapezoidal, and arrow-angle wings when attached mid-fuselage. Since the fuselage and tail remain unchanged, the wings show no significant pressure differences. The areas of highest pressure were identified at the nose of the fuselage, the leading edges of the wings, and where the tail bonds the fuselage. Conversely, the lowest pressure was noted at the front of the wing's upper surface camber. This area of low pressure is also visible in Figures 3.1, 3.2, and 3.3, which depict earlier pressure results.

Table 3.4: C_d and C_l values according to the connection position of the wing

Juncture	C_l	C_d	C_l/C_d
Rectangle from top	0.34433	0.038805	8.87334
Rectangle from the middle	0.37425	0.0381	9.82292
Trapezoidal from the middle	0.378266	0.03782	10.00121
Trapezoidal from below	0.2784	0.03939	7.06778
Arrow-angle from middle	0.35411	0.03777	9.37481
Arrow-angle from below	0.39897	0.0384	7.78567

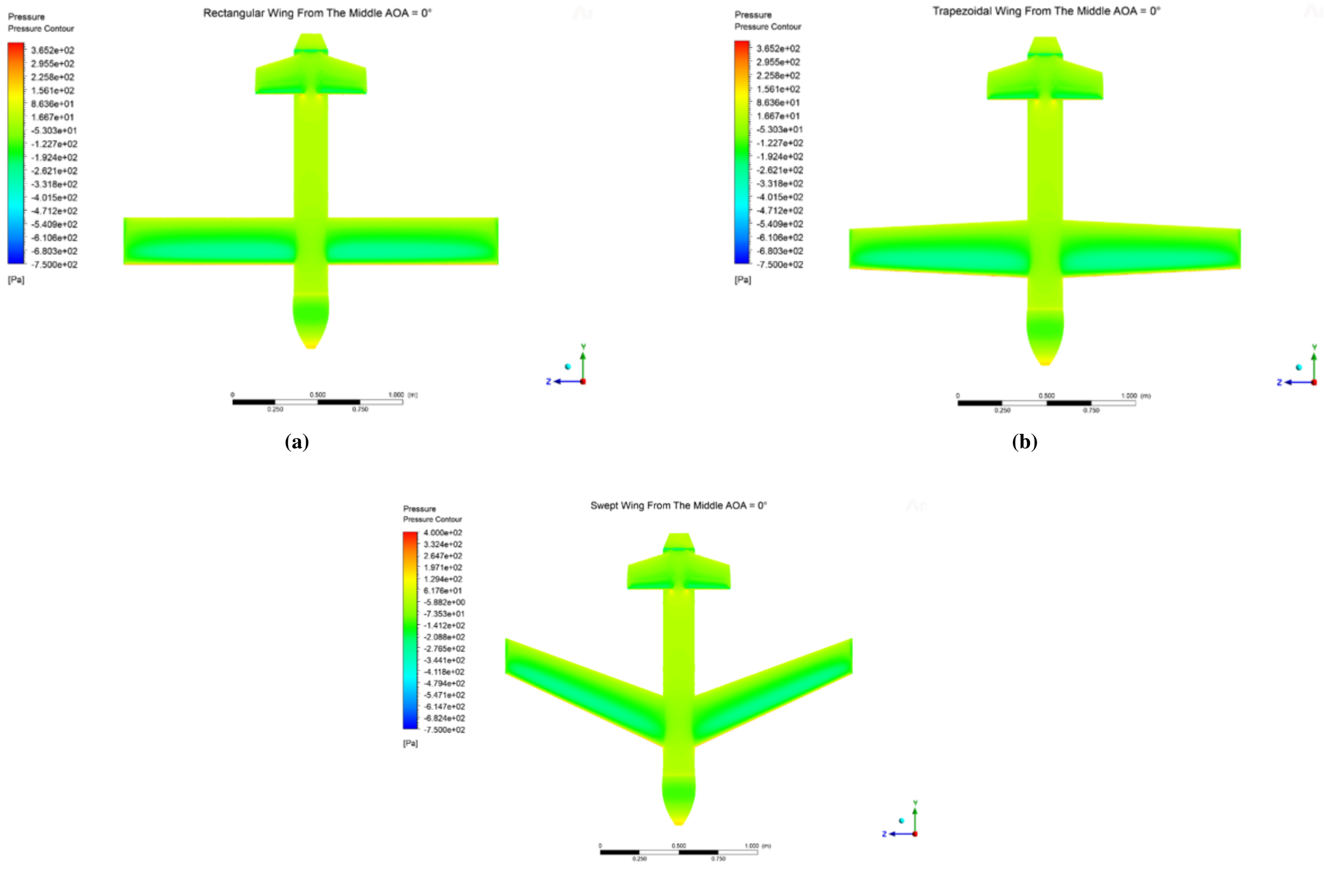

(a) **(b)**

(c)

Figure 3.13: Mid-Wing Rectangular, Trapezoidal, Arrow-Angle Pressure Distribution

3.7. Flight-cost calculation of Kamikaze *UAV* models

Based on ideal conditions, a basic flight-cost calculation for Kamikaze *UAVs* has been examined. Some assumptions and used values in the examinations made for rectangular and trapezoidal wings;

- Optimization values $C_{D\,\text{rectangular wing}} = 0.02089$
- Optimization values $C_{D\,\text{arrow-angle wing}} = 0.01976$
- The price of the fuel used, Kerosene, is 1 liter for Turkey = 1.154 dollar
- Kerosene fuel density $\rho = 0.82\,kg/L$
- Kerosene calorific value $(ID) = 46\ MJ/kg$
- Aircraft wing top view area $S = 0.55\ m^2$
- $V_s = 25\ m/s,\ \rho_{air} = 1.225\ kg/m^3$

- Aircraft engine efficiency $\eta = 85\%$
- Fuel calculation in dollars for 1 year of rectangular wing flight time;

$$\begin{aligned}
F_D &= (1/2)\,\rho.V_{\infty}^{2}.A.C_{D\,\text{rectangular wing}} \\
F_D &= (1/2)\ \times 1.225\ \times\ 25^2\ \times\ 0.02089 = 4.3997 \\
W_D &= F_D.V_{\infty} = 4.3997\left(\frac{kg.m}{s^2}\right)\times 25\left(\frac{m}{s}\right) = 109.9925\frac{kg.m^2}{s^3} \tag{3.1} \\
W_{motor} &= \frac{W_d}{\eta} = \frac{109.9925}{0.85} = 129.403\left(\frac{kg.m^2}{s^3}\right) \tag{3.2} \\
W_{motor} &= \dot{m}.ID = \rho\,.\dot{\forall}.ID \\
\dot{\forall} &= \frac{W_{motor}}{\rho_{fuel}.ID} = \frac{129.403\,\frac{kg.m^2}{s^3}}{0.82\,\frac{kg}{L}.46\frac{MJ}{kg}} = 3.431\ \times 10^{-6}\frac{L}{s} \\
\dot{\forall} &= 3.431\ \times 10^{-6}\frac{L}{s}.3600\frac{s}{h} = 0.0124\frac{L}{h}
\end{aligned}$$

for 8765 hours;

$$\begin{aligned}
0.0124\frac{L}{h}\ \times\ 8765h &= 108.686L \\
108.686\ \times\ 1.154 &= 125.424\text{ dollar}
\end{aligned}$$

Fuel calculation in dollars for 1 year of rectangular wing flight time;

$$\begin{aligned}
F_D &= (1/2)\,\rho.V_{\infty}^{2}.A.C_{D\,\text{arrow-angle wing}} \\
F_D &= (1/2)\ \times 1.225\ \times\ 25^2\ \times\ 0.01976 = 4.1604 \\
W_D &= F_D.V_{\infty} = 4.1604\left(\frac{kg.m}{s^2}\right)\times 25\left(\frac{m}{s}\right) = 104.01\frac{kg.m^2}{s^3} \\
W_{motor} &= \frac{W_d}{\eta} = \frac{104.01}{0.85} = 122.365\left(\frac{kg.m^2}{s^3}\right) \\
W_{motor} &= \dot{m}.ID = \rho\,.\dot{\forall}.ID \\
\dot{\forall} &= \frac{W_{motor}}{\rho_{fuel}.ID} = \frac{122.365\,\frac{kg.m^2}{s^3}}{0.82\,\frac{kg}{L}.46\frac{MJ}{kg}} = 3.244\ \times 10^{-6}\frac{L}{s} \\
\dot{\forall} &= 3.244 \times 10^{-6}\frac{L}{s}.3600\frac{s}{h} = 0.0117\frac{L}{h}
\end{aligned}$$

for 8765 hours;

$$\begin{aligned}
0.0117\frac{L}{h}\ \times\ 8765h &= 102.5505L \\
102.5505\ \times\ 1.154 &= 118.343\text{ dollar}
\end{aligned}$$

Arrow-angle kamikaze *UAV* was determined as the most suitable in flight-cost comparison.

4. Conclusions and Recommendations

In this study, the effects of wingspan shapes and wing-fuselage junction on the aerodynamic performance of an unmanned kamikaze aircraft were investigated. Three different wingspan models were used: trapezoidal, rectangular and arrow-angle shapes. The effects of angle of attack on the aerodynamic performance of different modelled unmanned aerial vehicles are shown. Pressure/velocity profiles and vortex formation results were obtained and the differences in the results were compared. C_l and C_d coefficients were obtained with the computational fluid mechanics analysis. The main findings found in the study can be summarized as follows.

Considering the pressure and velocity profiles and vortex formations, three different wing configurations were examined for kamikaze *UAVs* and the results of the effect of the angle of attack were given. C_l and C_d coefficients were obtained with the computational fluid mechanics analysis. The main findings found in the study can be summarized as follows;

- The structure of the pressures around the wings started to differ as a result of 15°. At 15°, the L– and L- negative pressure zones above the wing started to decrease in the rectangular and trapezoidal wing, while they increased in the arrow-angle wing.
- In the arrow-angle wing, according to other results, SP occurred at the rear and a low velocity profile without intense was formed.
- The lowest wingtip vortex formation occurred in the trapezoidal wing. When the vortex formations are examined, the arrow-angle wing structure creates a more appropriate distribution.

- When the location of the wing mounting to the fuselage and the type of wing were investigated, trapezoidal from the mid showed the most appropriate C_l/C_d performance.
- The trapezoidal wing has the highest lift coefficient up to 15° AoA. After 15°, the lift coefficient of both models started to decrease with the rectangular wing.
- While the arrow-angle wing exhibited the lowest lift coefficient behavior, the lift coefficient increased continuously up to 20°. There was no decrease in the lift coefficient.
- The drag coefficient increased in all models. The arrow-angle wing model has the lowest drag coefficient.
- The C_l/C_d ratio increased in all models up to 5° AoA. After 5° AoA, this ratio decreased in all wing models. While the trapezoidal wing has the highest ratio up to 14 ° AoA, the C_l/C_d ratio of the arrow angle model is higher at higher angles of attack.

While it is logical to use the trapezoidal wing up to 15° AoA. it is more appropriate to choose the arrow-angle wing model, which still increases the lift coefficient at higher angles of attack.

Article Information

Acknowledgements: The authors would like to express their sincere thanks to the editor and the anonymous reviewers for their helpful comments and suggestions.

Author's contributions: All authors contributed equally to the writing of this paper. All authors read and approved the final manuscript.

Conflict of interest disclosure: No potential conflict of interest was declared by authors.

Supporting/Supporting organizations: No grants were received from any public, private or non-profit organizations for this research.

Ethical approval: It is declared that during the preparation process of this study, scientific and ethical principles were followed and all the studies benefited from are stated in the bibliography.

Plagiarism statement: This article was scanned by the plagiarism program.

References

[1] J. Karimi, S. H. Pourtakdoust, *Optimal maneuver-based motion planning over terrain and threats using a dynamic hybrid PSO algorithm*, Aerosp. Sci. Technol., **26**(1) (2013), 60-71.
[2] J. P. Škrinjar, P. Škorput, M. Furdić, *Application of unmanned serial vehicles in logistic processes*, In New Technologies, Development and Application 4, Springer, 2019, 359-366.
[3] V. Hassija, et al., *A survey on IoT security: Application areas, security threats, and solution architectures*, IEEE Access, **7** (2019), 82721-82743.
[4] Y. Unpaprom, N. Dussadeeb, R. Ramaraj, *Modern Agriculture Drones, Modern Agriculture Drones Chapter: Modern Agriculture Drones the Development of Smart Farmers*, 2018, 13-19.
[5] I. Jeelani, M. Gheisari, *Safety challenges of UAV integration in construction: Conceptual analysis and future research roadmap*, Safety Science, **144** (2021), 105473.
[6] O. Adepoju, et al., *Drone/unmanned aerial vehicles (UAVs) technology, Re-skilling Human Resources for Construction 4.0: Implications for Industry*, Academia and Government, (2022), 65-89.
[7] F. Zeng, *Nested vehicle routing problem: Optimizing drone-truck surveillance operations*, Trans. Res. Part C: Emerging Tech., **139** (2022), 103645.
[8] P. Garg, et al., *Isdnet: Ai-enabled instance segmentation of aerial scenes for smart cities*, ACM Trans. Internet Tech. (TOIT), **21**(3) (2021), 1-18.
[9] A. Restas, *Drone applications for supporting disaster management*, World Journal of Engineering and Technology, **3**(3) (2015), 316-321.
[10] A. Straubinger, H.L. de Groot, E. T. Verhoef, *E-commerce, delivery drones and their impact on cities*, Transportation Research Part A: Policy and Practice, **178** (2023), 103841.
[11] H. Shakhatreh, et al., *Unmanned aerial vehicles (UAVs): A survey on civil applications and key research challenges*, IEEE Access, **7** (2019), 48572-48634.
[12] S. A. Hoseini, et al. *Trajectory optimization of flying energy sources using q-learning to recharge hotspot UAVs*, in IEEE INFOCOm 2020-IEEE conference on computer communications workshops (INFOCOm WKSHPS), 2020, IEEE, 683-688.
[13] M. Prieto, M.S. Escarti-Guillem, S. Hoyas, *Aerodynamic optimization of a VTOL drone using winglets, Results in Engineering*, **17** (2023) 100855.
[14] V. Chamola, et al., *A comprehensive review of the COVID-19 pandemic and the role of IoT, drones, AI, blockchain, and 5G in managing its impact*, IEEE Access, 8 (2020), 90225-90265.
[15] K. Li, et al., *Energy efficient legitimate wireless surveillance of UAV communications*, IEEE Transactions on Vehicular Technology, **68**(3) (2019), 2283-2293.
[16] G. Bai, et al., *Network approach for resilience evaluation of a UAV swarm by considering communication limits*, Reliability Engineering & System Safety, **193** (2020), 106602.
[17] S. R. Edulakanti, S. Ganguly, *The emerging drone technology and the advancement of the Indian drone business industry*, The Journal of High Technology Management Research, **34**(2) (2023), 100464.
[18] S.G. Kontogiannis, J.A. Ekaterinaris, *Design, performance evaluation and optimization of a UAV*, Aerosp. Sci. Technol., **29**(1) (2013), 339-350.
[19] C. Fu, et al., *Adaptive robust backstepping attitude control for a multi-rotor unmanned aerial vehicle with time-varying output constraints*, Aerosp. Sci. Technol., 78 (2018), 593-603.
[20] P. Panagiotou, K. Yakinthos, *Aerodynamic efficiency and performance enhancement of fixed-wing UAVs*, Aerosp. Sci. Technol., 99 (2020), 105575.
[21] J. Anderson, *EBOOK: Fundamentals of Aerodynamics (SI units)*, McGraw Hill, 2011.
[22] A. Quintana, et al., *Aerodynamic analysis and structural integrity for optimal performance of sweeping and spanning morphing unmanned air vehicles*, Aerosp. Sci. Technol., **110** (2021), 106458.
[23] M. Voskuijl, *Performance analysis and design of loitering munitions: A comprehensive technical survey of recent developments*, Defence Technology, **18**(3) (2022), 325-343.
[24] D. Zampronha, A. Albuquerque, *Cheaper Precision Weapons: An Exploratory Study about the HESA Shahed 136*, Advances in Aerosp. Sci. Technol., **9**(1) (2024), 40-59.
[25] T. Saraçyakupoğlu, H. D. Delibaş, A. D. Özçelik, *An experimental determination and numerical analysis of a loiter munition unmanned aerial vehicle system*, International Journal of 3D Printing Technologies and Digital Industry, **6**(1) (2022), 83-101.
[26] E. Sakarya, A. Alkan, *Savunma sanayiinde kullanilabilecek Kamikaze İha uygulaması*, Bilgisayar Bilimleri ve Teknolojileri Dergisi, **2**(1) (2021), 24-28.
[27] A. Sadikin, et al., *A comparative study of turbulence models on aerodynamics characteristics of a NACA0012 airfoil*, International Journal of Integrated Engineering, **10**(1) (2018).
[28] C. Suvanjumrat, *Comparison of turbulence models for flow past NACA0015 airfoil using OpenFOAM*, Engineering J., **21**(3) (2017), 207-221.